Thermally Chargeable Ammonium-Ion Capacitor for Energy Storage and Low-Grade Heat Harvesting

Yufeng An,[a] Zhiwei Li,[a] Yao Sun,[a] Shaopeng Li,[a] Yinghong Xu,[a] Hui Dou,[a] and Xiaogang Zhang*[a]

Harvesting heat from the low-grade heat (below 100 °C) into electricity has the signification to enhance the utilization of energy and lower carbon emissions by a simple device. Herein we demonstrate a thermally chargeable ammonium ion capacitor (TAIC) by employing graphene-polyimide (rGO-PI) synthesized through polycondensation of 1,4,5,8-naphthalene-tetracarboxylic dianhydride and ethylenediamine as cold electrode, N-doped hollow carbon nanofibers as hot electrode to directly convert waste heat into electricity. Combining thermo-diffusion effect of electrolyte with thermogalvanic effect of a redox couple ($-C=O/-C-O-NH_4^+$), as-assembled TAIC can deliver a high output voltage of 624 mV, power density of 82 $\mu W\,cm^{-2}$ and average Seebeck coefficient of 9.07 $mV\,K^{-1}$ at temperature difference of 45 K. Meanwhile, with the introduction of polyacrylamide-polyacrylic acid-based gel electrolyte, the assembled flexible device can well serve in various bending states, and the power density can attain a satisfying value of 1.92 $\mu W\,cm^{-2}$. This quasi-solid-state TAIC shows great potential as one promising candidate for high value-added conversion from low-grade heat into electricity as well as wearable applications.

Introduction

Environmental issues caused by the continuous consumption of traditional fossil energy sources become more serious, so the implementation of the global carbon neutrality strategy is no time to delay.[1–5] Consequently, it is especially important to develop and use green and sustainable energy. The survey results show that 72% of the global primary energy is lost during use, of which 63% is accounted for low-grade waste heat energy below 100 °C.[6–10] This low-grade waste heat energy is usually released directly into the environment, leading to energy waste and also generating certain environmental issues such as the greenhouse effect.[8,11,12] It is estimated that the efficient use of waste energy would reduce energy demand by about 12% and greenhouse gas emissions such as CO_2 by about 13%, which would not only improve energy efficiency but also curb environmental degradation.[13,14] However, it is difficult for conventional thermoelectric devices to efficiently obtain waste energy at low temperatures (< 100 °C). Therefore, based on the new thermoelectric convention concept, it is essential to develop a practical device with higher conversion efficiency that is simple and convenient to convert thermal energy to electrical energy directly using the temperature difference.

Conventional thermoelectric devices in the form of ions diffusion caused by temperature gradients have been extensively studied and have made great progress in terms of thermoelectric conversion performance.[12,15,16] However, the inherently low Seebeck coefficient (S) limits their further practical application, usually, the S of the conventional thermoelectric devices is only 10–200 $\mu V\,K^{-1}$.[12,17] Recently, some significative works acquired an enhanced S have been reported. Crispin's group reported an ionic thermoelectric supercapacitor driven by temperature gradient, the S value is reached 10 $mV\,K^{-1}$ originated from ionic Soret effect of liquid state polymeric electrolyte.[18] Peljo et al. developed a thermally regenerative copper nanoslurry flow battery, it can disburse an extremely high power density (up 150 $W\,m^{-2}$) by adding Cu(I) complex into electrolyte that can occur redox reaction to effectively increase the power density.[11] Many excellent works have been reported, nevertheless, most of them are only based on electrolyte and at the level of thermal charging capacitors based on electric double layer mechanism, where in-depth studies and reports on electrode materials are relatively deficient. The physicochemical properties of electrode materials directly determine the output power and energy density of thermoelectric conversion devices.[17,19,20] Therefore, the most advisable strategy would be to develop electrode materials with high performance for thermoelectric conversion devices.

As a special engineering material, Polyimide (PI) has been widely used in microelectronics, separation film, aviation, aerospace and other fields due to its outstanding characteristic of thermal stability, mechanical strength and nontoxicity.[21,22] In recent years, the PI has been explored as an energy storage material because of its electroactive redox groups (the imide ring, $-CO-N-CO-$) and simple preparation method.[23–25] Zhang et al. confirmed that NH_4^+ is a more appropriate substitute as a

[a] Y. An, Z. Li, Y. Sun, S. Li, Y. Xu, Prof. H. Dou, Prof. X. Zhang
Jiangsu Key Laboratory of Electrochemical Energy Storage Technologies
College of Materials Science and Technology
Nanjing University of Aeronautics and Astronautics
Nanjing, 210016, China
E-mail: azhangxg@nuaa.edu.cn
Supporting information for this article is available on the WWW under https://doi.org/10.1002/batt.202200036

charge carrier for PI electrode compared to Na$^+$ and Li$^+$. Meanwhile, the PI as an *n*-type semiconductor material, the carriers (electrons/holes) in the semiconductor are affected by the temperature gradient during the heating process and will move from the hot end to the cold end, in which an electric potential will be generated in the circuit.[21,26] However, the relatively low conductivity of PI leads to low thermoelectric effect compared to conventional thermoelectric conversion materials. For materials of thermoelectric conversion, the figure of merit can be defined as Equation (1):[17,27]

$$ZT = TS^2\sigma/k \tag{1}$$

where *T*, *S*, σ and *k* are the temperature, the Seebeck coefficient, the electric conductivity and the thermal conductivity, respectively.

Based on this relation, the enhanced conversion efficiency of thermoelectric materials can be achieved by increasing *S*, σ and reducing *k*. In order to optimize *ZT*, electrons must experience very little scattering rate, ensuring high electro-conductivity (as in a crystal), conversely, phonons must suffer a high scattering rate, thus decreasing thermal conductivity [like in a glass].[28,29] However, both the electrical and thermal conductivity of materials are carrier-dependent.[10,28] As far as the present study is concerned, widening the rate between

electrical and thermal conductivity as much as possible is an effective means to improve the heat-to-electric conversion efficiency. Graphene, with its unique two-dimensional structure (consisting of a dense layer of carbon atoms wrapped in a honeycomb array of crystalline dots in *sp^2* heterojunction), has both high thermal and electric conductivity, which appears to be detrimental to thermoelectric conversion efficiency.[28,30] However, the rate between electrical and thermal conductivity be reached 3 (electric conductivity is 15000 cm^{2}V^{-1}S^{-1}, thermally conductive is 5000 Wm^{-1}K^{-1}), the *ZT* is about 3.25.[28,30] Electrons move through the orbitals without scattering due to the lattice defects or the introduction of foreign atoms.[28,31] In addition, graphene can form a connected conductive structure without other auxiliary materials because of its π-π stacking interactions. Therefore, a hybrid structure made of PI and graphene would be a viable option to development of high-performance thermoelectric devices.

Based on the analysis of the test results and the corresponding literature reports,[12,15,16] a possible synergetic thermoelectric conversion mechanism between the thermodiffusion and thermogalvanic effect is described in Figure 1. When no heat source is provided, graphene-polyimide (rGO-PI) and N-doped carbon nanofiber (NCNF) electrodes are at the same temperature without temperature difference, and the device system is in equilibrium, so no output voltage is generated
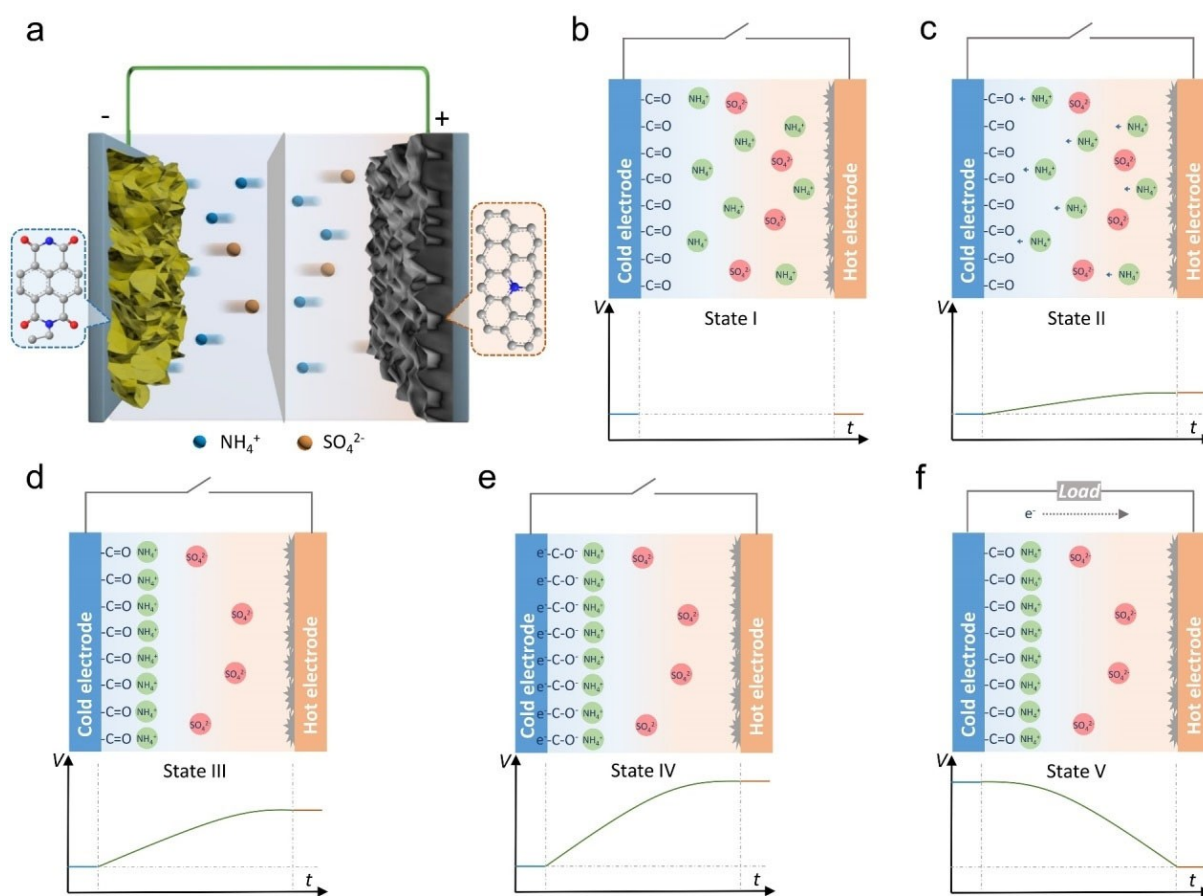
Figure 1. a) The diagrammatic sketch of electrochemical reaction mechanism. b) Initial state, c, d) thermodiffusion effect, e) thermogalvanic effect and f) load discharge.

(state I). When heat (thermal energy) is exerted NCNF electrode, the temperature gradient causes thermal diffusion of NH_4^+ from hot side (NCNF electrode) to cold side (rGO-PI electrode) due to the cations have a higher diffusion coefficient (state II). As a consequence, the thermal diffusion of NH_4^+ accumulates positive net charges near the rGO-PI electrode, generating a thermal-diffusive voltage (state III). Subsequently, the thermal-diffusive voltage can drive a reduction reaction between rGO-PI and NH_4^+ to acquire electron at cold side (rGO-PI electrode), which can increase the output voltage (state IV). Finally, the device undergoes a discharge process when the external load is connected (state V).

Herein, we propose and develop promising thermally chargeable ammonium ion capacitor by combining rGO-PI anode and NCNF cathode. The unique rGO-PI composite, prepared through a polycondensation reaction of dianhydride and diamine at high temperature, is employed as sensitive thermoelectric material to directly utilize low-grade waste heat. The NCNF with hollow microstructure can greatly shorten the diffusion pathway and enhance the penetration of electrolyte ions. As-assembled asymmetrical ammonium ion capacitor (AAIC) exhibits excellent electrochemical performance including a maximum energy density of 45.9 $Wh\,kg^{-1}$ and a maximum power density of 45.0 $kW\,kg^{-1}$. Additionally, the thermally chargeable ammonium ion capacitor (TAIC) delivers a satisfying average α value of 9.07 $mV\,K^{-1}$ and a large output power density of 82 $\mu W\,cm^{-2}$ at a temperature difference of 45 K.

Results and Discussion

As illustrated in Figure 2(a), we adopted an in-situ polymerization strategy to prepare rGO-PI composite material (detail in Experimental section). Briefly, NTCDA and EDA monomers can absorb on the surface of GO, and then form polymer chains through a polycondensation reaction at high temperature (Figure S1).[21,22] The well dispersed graphene not only acts as continuous electron transport pathway and but also provides intimate contact with polymer, which could improve the thermoelectric conversion efficiency ZT [based on Equation (1)] and accelerate charge transfer.

Figure 2(b and c) is SEM images of PI and rGO-PI, respectively. It can observe that PI is formed by stacking of small lamellae with serious agglomeration. In contrast, the introduction of graphene dramatically hinders the stack of PI, which is beneficial for the characteristics of composite material
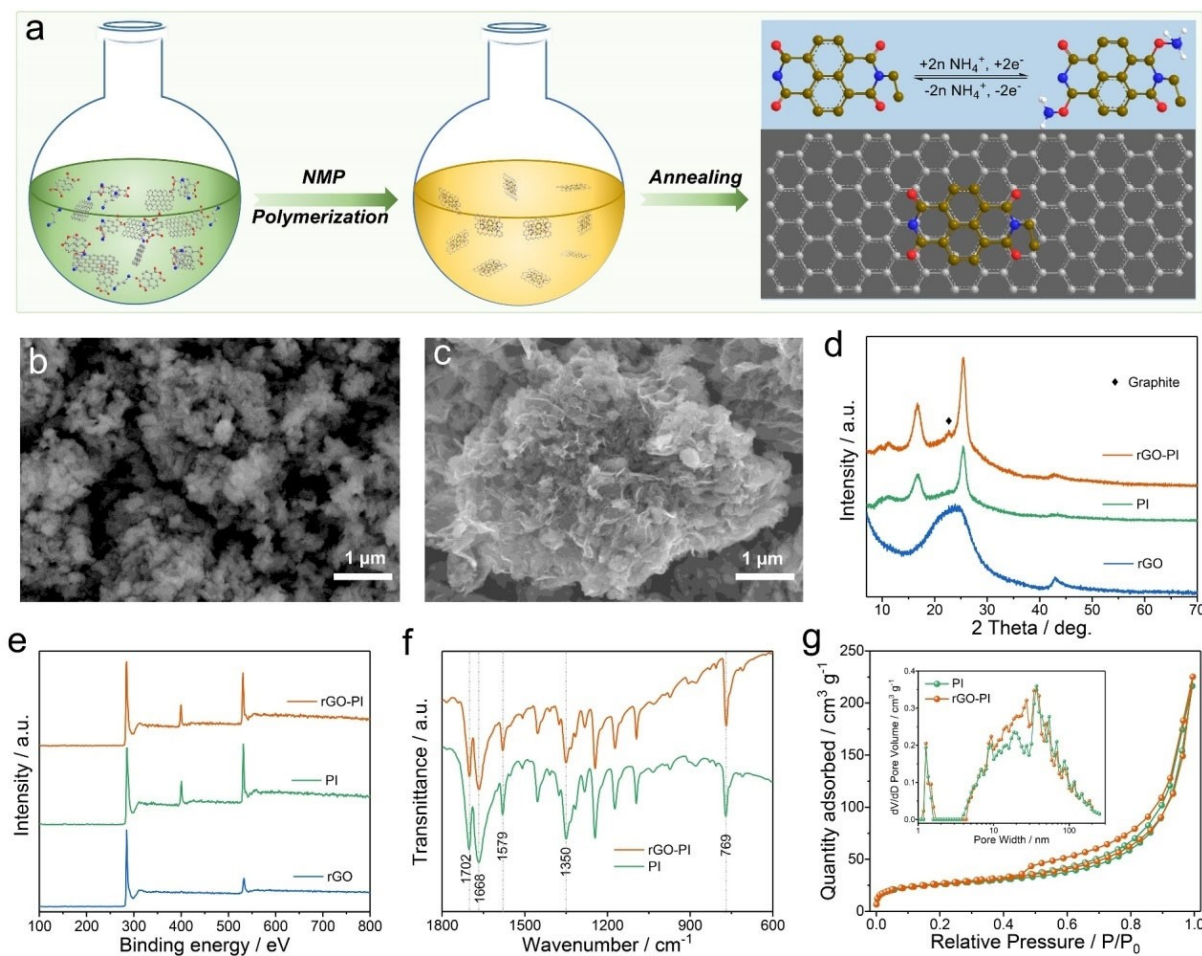
Figure 2. a) Schematic preparation of rGO-PI. b, c) SEM images of PI and rGO-PI. d) XRD patterns, e) XPS survey spectra, f) FT-IR spectra and g) N$_2$ adsorption-desorption isotherms and pore size distribution curves.

including the diffusion of electrolyte ions and the thermo-electric conversion efficiency. As determined by the XRD spectra in Figure 2(d), there are no new peaks in the XRD spectrum of rGO-PI except for the characteristic peaks of rGO and PI, indicating that no byproducts are exhibited in as-obtained material. It is worth noting that the (002) plane of graphite in rGO-PI shows a slight negative shift compared with rGO, indicating the expansion of rGO layer spacing attributed to the insertion of PI between rGO layers.[32,33] Importantly, for the peak at around 16.9° and 25.8°, the intensity of rGF-PI was higher than that of pure PI, indicating that the graphene substrate can increase the crystallinity of the in-situ grown PI polymer probably via π-π interaction.

The chemical composition of sample was analyzed by XPS. As summarized in Figure 2(e), both PI and rGO-PI are composed of C, N, and O elements, while N element does not appear in pure rGO. Compared with PI, the content of C element increases, and the contents of N and O element decrease in rGO-PI, which is caused by the introduction of graphene (Table 1). The structural compositions of PI and rGO-PI were further characterized by FT-IR spectra, as plotted in Figure 2(f). The peaks located at 1350 cm^{-1} and 1579 cm^{-1} can be attributed to the stretching vibration of the C−N bond and the naphthalene ring, respectively. The peaks at 1702, 1668 and 769 cm^{-1} represent the vibrations of the amide C=O bond.[21,34] According to the nitrogen adsorption and desorption and pore size distribution curves of samples (Figure 2g). The specific surface areas of rGO-PI and PI are almost equal (Table 1), but the curve of rGO-PI has a larger hysteresis loop at a relative pressure of 0.4–1.0, and the corresponding pore size distribution curve of rGO-PI has a larger adsorption volume, indicating that rGO-PI has a loose structure, which is consistent with the SEM observation.

To evaluate the electrochemical performance of the materials, we firstly performed a series of tests. As shown in Figure 3(a), the integrated area of CV curve for rGO is far smaller than that of rGO-PI and PI, indicating its negligible capacity contribution in rGO-PI composite. Notably, two pairs of redox peaks appeared in both CV curves for rGO-PI and PI can be corresponding to the two-step enolization reaction of PI (−C=O→−C−O−NH$_4^+$).[21,23] Moreover, the potential gap between redox peaks of rGO-PI is relatively smaller than that of PI, implying the lower polarization of rGO-PI electrode. Figure 3(b) shows the specific capacity performance of PI and rGO-PI at current densities of 0.5, 1, 2, 5, 10, 20, 50 and 100 A g^{-1}, the specific capacity of PI and rGO-PI is 154.4, 149.5, 145.9, 141.3, 134.4, 124.5, 85.5 60.6 mAh g^{-1} and 163.7, 159.9, 156.7, 153.1, 148.5, 143.2, 120.5, 99.8 mAh g^{-1}, respectively. In addition, the theoretical capacity of PI can be calculated as 183.4 mAh g^{-1}

(reactions based on two electrons). Under this case, the utilization rate of PI is 84.2%, while that of rGO-PI can be as high as 99.2% (the mass of PI in the rGO-PI composite is calculated at 90%). When the current density is increased by 200 times, the specific capacity of rGO-PI can still be maintained at 61.0%, while the PI electrode can only be maintained at 39.3%. Such result indicates that the introduction of rGO can not only greatly improve the structure stability, but also enhance the electrochemical performance of electrode materials. As shown in EIS spectra (Figure 3c), rGO-PI has a smaller equivalent series resistance, a smaller charge migration resistance and a more pronounced capacitive behavior, exhibiting a faster kinetic process. The inset in Figure 3(c) shows the Bode plots of both electrodes. Compared with PI, rGO-PI exhibits a phase angle (∼−90°), which is much closer to that of an ideal capacitive material. As a result, the time constants τ_0 ($\tau_0 = 1/f_0$) of PI and rGO-PI can be obtained as 2.9 and 0.9 s, respectively. Besides, the Tafel slopes (Figure 3d) of PI and rGO-PI during redox are 200.3, −255.5 mV dec^{-1} and 115.2, −161.8 mV dec^{-1}, respectively. The smaller Tafel slope of rGO-PI than that of PI further illustrates its fast redox response, which is in line with the results of CV and rate capability. The excellent performance of rGO-PI can be attributed to the efficient integration of in-situ grown PI with the graphene substrate, which facilitate rapid charge transfer and NH$_4^+$ diffusion that are beneficial to the fast and complete redox reaction of the PI polymer. Figure 3(e) shows the CV curves of the rGO-PI electrode in (NH$_4$)$_2$SO$_4$ electrolyte at different scan rates. It can be found that the current response of the CV curve increases with the increasement of scan rate, but the shape remains basically unchanged. In contrast, the oxidation peaks in the CV curves of PI at different scan rates shift to the right and the corresponding reduction peaks shift to the left (Figure S3), indicating that rGO-PI electrode has a smaller polarization. Figure 3f shows the charging and discharging curves of rGO-PI at various current densities. It is worth mentioning that the Coulomb efficiency of the electrode can remain a high value over 98%, indicating a high reversibility. To further study the kinetic behavior of the electrode material, we fitted the relationship between peak current (i_p) and scan rate (v), according to Equations (2) and (3):[35,36]
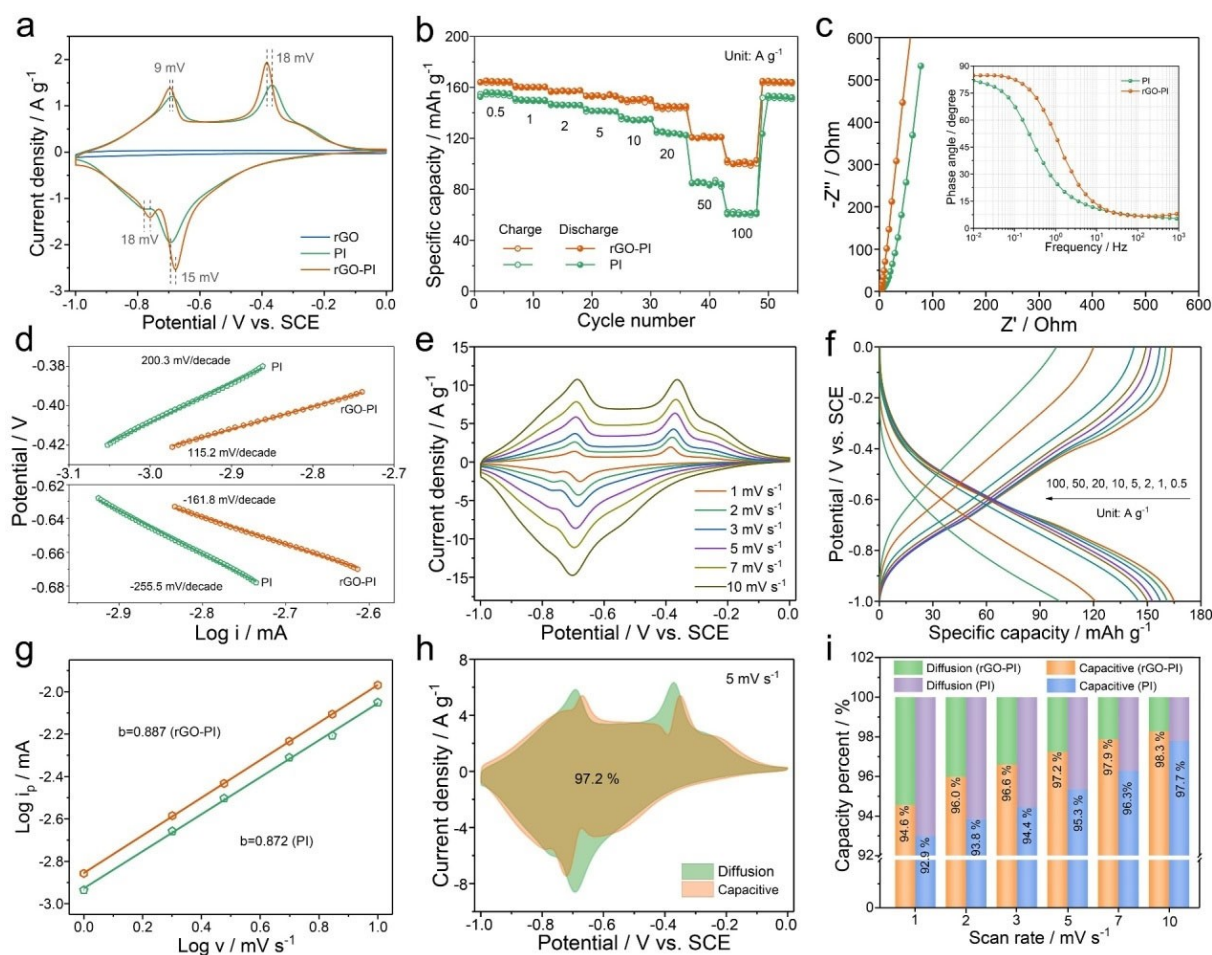
$$i = av^b \tag{2}$$

$$\log i = b \log v + \log a \tag{3}$$

where a and b are adjustable parameters. In particular, when $b = 0.5$ or 1, the electrochemical reactions are controlled by diffusion or capacitive behavior, respectively. The fitted slopes

Table 1. Physical parameters of rGO-PI and PI.

Sample	SSA [m^2 g^{-1}]	Element [%]			Thermal diffusivity [mm^2 s^{-1}]	Electrical conductivity [S cm^{-1}]	S [mV K^{-1}]
		C	N	O			
PI	86.1	66.3	12.7	21.0	0.141	1.253×10^{-9}	8.85
rGO-PI	88.4	69.3	11.2	19.5	0.202	3.425×10^{-4}	9.07

Batteries & Supercaps

Research Article
doi.org/10.1002/batt.202200036

Chemistry Europe
European Chemical
Societies Publishing

Figure 3. a) CV curves at a scan rate of 1 mV s^{-1}, b) rate capability, c) EIS spectra, d) Tafel slopes, e) CV curves at different scan rates and f) charge-discharge curves at different current densities of rGO-PI. g) b-values, h) contribution of the capacitive behavior of rGO-PI at 5 mV s^{-1} and i) capacitive and diffusion behavior 1 to 10 mV s^{-1}.

of the right oxidation peaks for the PI and rGO-PI electrodes were 0.872 and 0.887, respectively (Figure 3g), indicating that both PI and rGO-PI are dominated by capacitive behavior. Moreover, the electrochemical surface reaction current (k_1v) and diffusion-controlled current ($k_2v^{1/2}$) contributions are further analyzed by analyzing the CV curves according to the following equations:[36,37]

$$i = k_1v + k_2v^{1/2} \tag{4}$$

The contribution of the surface controlled and diffusion-controlled currents to the total current at a given potential can be obtained by determining the values of k_1 and k_2, respectively. As shown in Figure 3(h), the shaded part of the CV curve represents the capacitive contribution of the surface control. For example, at a scan rate of 5 mV s^{-1}, the capacitive contribution of the rGO-PI electrode is 97.2%. A plot of the quantitative capacitive contribution versus the scan rate was shown in Figure 3(i). It can be seen that the capacitive contributions of both PI and rGO-PI electrodes are above 90% at different scan rates, meaning the surface redox reactions of PI and rGO-PI, while the capacitive contribution of rGO-PI

electrode is higher. From the electrochemical test analysis, it can be confirmed that the introduction of rGO improves the utilization rate of rGO-PI, promotes the current response capability, and accelerates the rate of redox reaction.

In order to evaluate the ability of harvesting low-grade heat, we assembled firstly an aqueous ammonium ion capacitor (AAIC) by using as-prepared negative electrodes (rGO, PI, and rGO-PI), N-doped hollow carbon nanofibers (NCNF) positive electrode and (NH$_4$)$_2$SO$_4$ electrolyte (Figure S8). As-prepared NCNF shows a nanodots engineered one-dimensional hollow nanofibers micromorphology, which can provide larger specific surface area and shorten the diffusion path of electrolyte ions (Figure S6).[38] The specific capacitance of NCNF electrode is up to 152 F g^{-1} at a current density of 1 A g^{-1} (Figure S7). On the basis of the electrochemical performance of rGO-PI and NCNF, the maximum work voltage of AAIC is forecasted to be 2.0 V. Various CV tests with different voltage ranges were employed to identify the optimum working voltage (Figure S9a). When the test voltage increases to a higher 1.9 or even 2.0 V, there is obvious polarization. Thus, we choose 1.8 V as the optimal voltage window to further assessment the electrochemical performance of the AAIC. As profiled in Figure S9(b), the GCD

Batteries & Supercaps

Research Article
doi.org/10.1002/batt.202200036

**Chemistry
Europe**
European Chemical
Societies Publishing

curves of AAIC at different current densities from 0.5 to 50 A g^{-1} exhibit symmetric quasi-triangular shapes, demonstrating its high reversibility. The specific capacitance of the rGO-PI//NCNF AAIC is measured to be 102, 100, 98, 94.8, 91.2, 86 and 69.6 F g^{-1} at 0.5, 1, 2, 5, 10, 20 and 50 A g^{-1}, respectively. Capacitance retention up to 68.2% when current density is increased by a factor of 100. The rate capability of rGO-PI//NCNF AAIC is obviously better than that (41 F g^{-1} at 0.5 A g^{-1}, 40.6% retention relative to 50 A g^{-1}) of the PI//NCNF AAIC (Figure S9c). Figure S9(d) shows the EIS plots of both AAIC. The semicircle in the high frequency region represents the charge transfer resistance (R_{ct}) of the electrode reaction. It can be seen that the rGO-PI//NCNF AAIC has a smaller R_{ct} value compared to the PI//NCNF AAIC, indicating that the introduction of rGO accelerates the charge transfer in the reaction. In addition, the more vertical straight line in the low frequency region responds to the faster kinetic of NH4$^+$ for rGO-PI//NCNF AAIC. The Ragone plot (Figure S9f) shows that the designed rGO-PI/NCNF AAIC has excellent output energy and power. A high energy density of 45.9 Wh kg^{-1} (based on the total active mass of both electrodes) is achieved at the power density of 450 W kg^{-1}. Even at a high-power density of 45 kW kg^{-1}, the rGO-PI//NCNF AAIC still possesses an energy density of 31.3 Wh kg^{-1}. As shown in Figure S9(f), compared with other reported capacitors in aqueous and non-aqueous systems, such as nitrogen-rich biomass carbon//LiMn$_2$O$_4$ LIC (17 Wh kg^{-1}, 6900 W kg^{-1}),[39] carbon based potassium ion battery-supercapacitor hybrid device (13.3 Wh kg^{-1}, 599 W kg^{-1}),[5] PI//PTMA (9 Wh kg^{-1}, 10 kW kg^{-1}),[24] OECG//Nb$_{18}$W$_{16}$O$_{93}$ (41.9 Wh kg^{-1}, 170.6 W kg^{-1}),[40] rGO@VO$_2$//AC (15.2 Wh kg^{-1}, 10 kW kg^{-1}),[41] LiMn$_2$O$_4$//AC (10.7 Wh kg^{-1}, 491 W kg^{-1}),[42] porous hollow carbon spheres PIHC (19.1 Wh kg^{-1}, 8203 W kg^{-1}),[43] AC//LTO

(27 Wh kg^{-1}, 3200 W kg^{-1}),[44] PI//methylene blue (15 Wh kg^{-1}, 19 kW kg^{-1}),[34] symmetric Th-GA (32.6 Wh kg^{-1}, 753 W kg^{-1}),[45] our rGO-PI//NCNF AAIC shows great competitivity. Cyclic stability tests were performed at 5 A g^{-1}, with a capacity retention of almost 94.2% up to 10,000 cycles for rGO-PI//NCNF AAIC (Figure S10), which is better than that PI//NCNF AAIC (62.6%).

Furthermore, we adopted a non-isothermal H-type configuration to evaluate the ability for converting low-grade thermal energy to electricity, which uses N-doped hollow carbon nanofibers (NCNF) electrode as hot side, rGO-PI electrode as cold side and 1 mol L^{-1} (NH$_4$)$_2$SO$_4$ as electrolyte (as shown in Figure 4a), respectively. During the experiment NCNF electrode was heated in an adjustable hot bath to obtain a temperature difference (ΔT) and ΔT was measured by thermometer of in close proximity to the electrode/electrolyte interface. The output voltage of TAIC was recorded as a function of time throughout the electrochemical workstation at a series of ΔT (Figure 4b). In the primary stage, both electrodes are at room temperature ($\Delta T = 0$ K), so, the corresponding output voltage is almost 0 V. With the gradual input of heat, a temperature difference is gradually generated between the two electrodes, and ΔV shows the increased behavior with temperature. When the temperature difference reaches 45 K, the output voltage gradually stabilized. At this time, the output voltage of rGO-PI can reach 624 mV, and the corresponding S-factor can be 9.07 mV K^{-1}, which is higher than the output voltage (508 mV) and S-factor (8.85 mV K^{-1}) of PI (Figure 4c). Obviously, during the initial ramp-up phase, a more vertical slope of rGO-PI than PI illustrates a faster response rate to electrolyte ions. We also replaced rGO-PI with a pristine rGO electrode as the cold side and NCNF as the hot side. The results show that the output
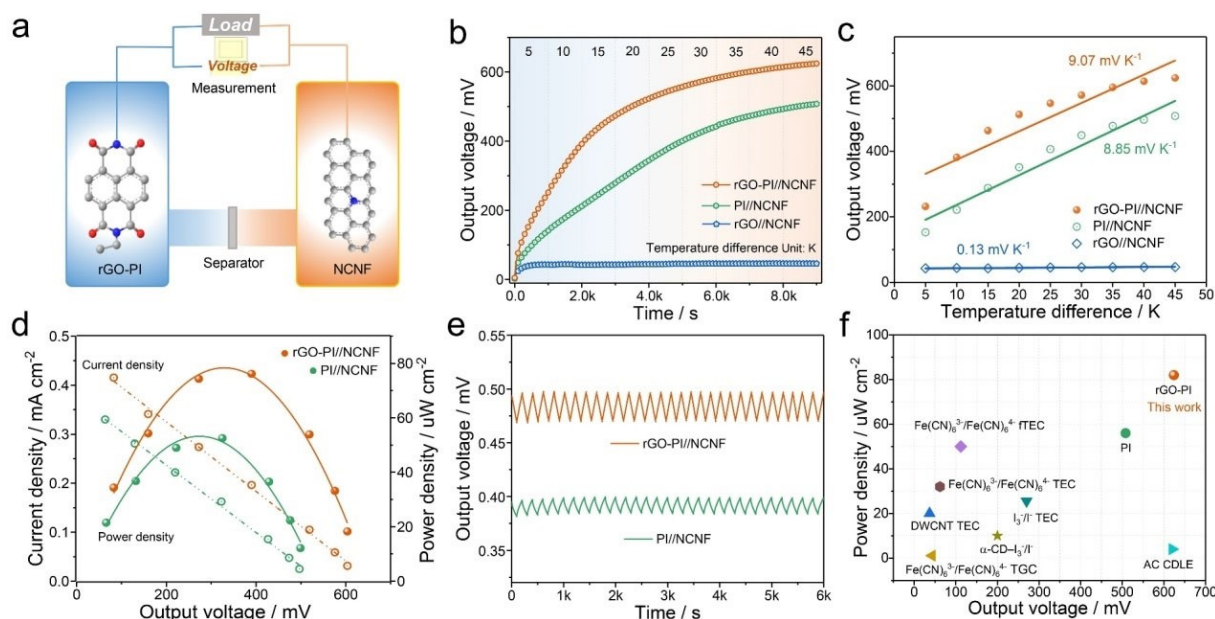
Figure 4. Thermoelectric conversion performance: a) schematic illustration, b) thermally charging process, c) a summary of ΔV at each temperature difference, d) plots of power and current density versus output voltage for the various load resistances at ΔT of 45 K and e) reproducible output voltage under 30 repeated charge-discharge with a load. (f) Performance comparison.

Batteries & Supercaps

Research Article
doi.org/10.1002/batt.202200036

Chemistry Europe
European Chemical
Societies Publishing

voltage of rGO is only 46.7 mV with an *S*-factor of 0.13 mV K^{-1} because of its surface adsorption behavior and small specific surface area. The above results indicate that the introduction of rGO makes a very positive contribution to fast response of electrolyte diffusion and voltage output. To further evaluate the thermoelectric energy conversion performance, we tested the discharge performance by loading different resistances and calculated the corresponding current density and power density, as shown in Figure 4(d). The maximum power density of rGO-PI//NCNF TAIC is 82 μW cm^{-2}, which is higher than that of PI//NCNF device (50 μW cm^{-2}). The thermal charging repetition performance of the device was tested by repeated thermal charging and load discharging at a temperature difference of 45 K. As shown in Figure 4(e), after 30 cycles of repeated charge-discharge, the output voltage still can be well maintained, which indicates that the device has good thermal charging stability. As shown in figure 4f, the output voltage and power density of our device are desirable when compared with other reported systems (more detailed information is listed in Table S1).[20,46–51]

Density functional theory (DFT) was employed to determine the Gibbs free energy of the electrochemical reaction between electrode and NH$_4^+$, as shown in Figure 5. There is a lower free energy (-11.634 eV) for rGO-PI composites compared with pure PI (-10.613 eV), demonstrating that the redox reaction is more easily to take place for rGO-PI. Such results further imply a faster electrochemical response, superior rate capability and smaller polarization. Moreover, the involved redox reaction can spontaneously proceed under the existence of temperature difference due to $\Delta G < 0$. Under this case, the output voltage for PI-based systems could be stabilized when the reduction reaction tends to a balanced state (Figure S11). In addition, the charge can be released *via* the oxidation reaction of PI. When considering external load, the voltage change caused by reversible redox reaction could realize the continuous conversion from low-grade heat to electricity.

To determine the rate of the thermally charging, we collected the galvanostatic discharge curves of such thermally charged cell under 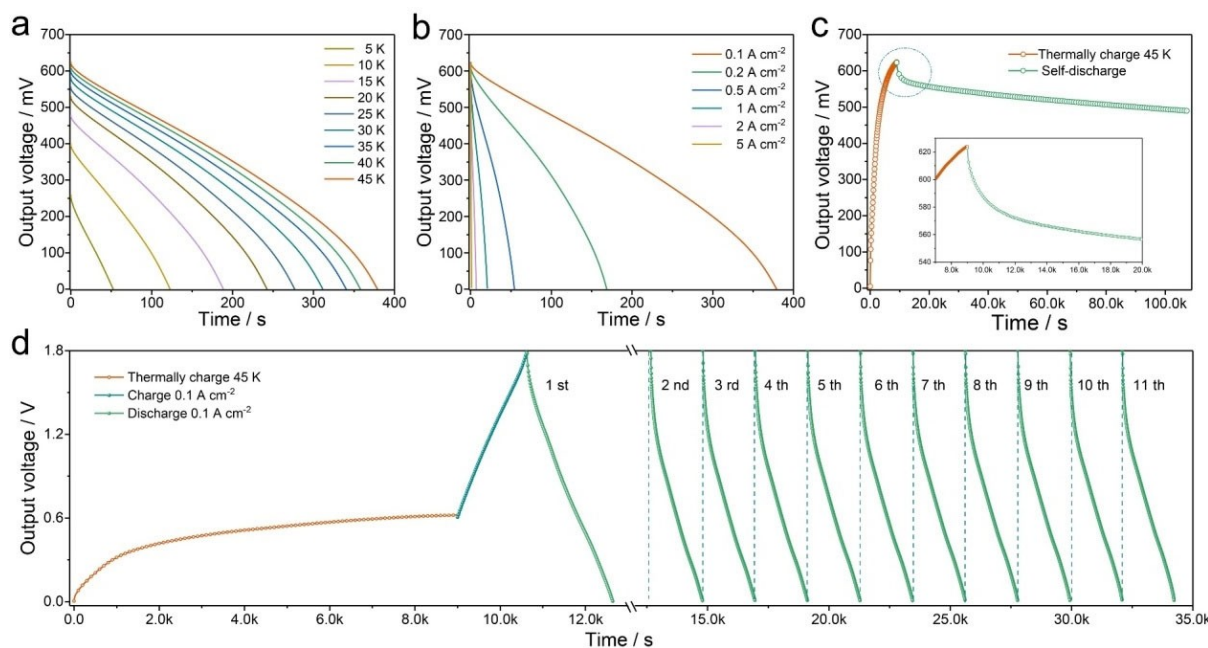various temperature differences. As marked in Figure 6(a), a specific capacitance is 20 F cm^{-2} can be obtained at 0.1 A cm^{-2} with a temperature difference of 5 K. The specific capacitance further increases to 53 F cm^{-2} with a higher temperature difference of 30 K. When the temperature difference extends to 45 K, the specific capacitance reaches a value as high as 61.3 F cm^{-2}. The rate capability of the thermally charging cell was also investigated under a temperature difference of 45 K, as shown in Figure 6(b). As-constructed rGO-PI//NCNF TAIC can deliver specific capacitances of 61.3, 54.5, 43.5, 33.4, 22.3 and 9.7 F cm^{-2} at current densities of 0.1, 0.2, 0.5, 1.0, 2.0 and 5.0 A cm^{-2}, respectively. Figure 6(c) shows the self-discharge phenomenon of TAIC after eliminating the temperature difference. Notably, a high open circuit voltage of 624 mV can be achieved with thermal charging at 45 K. When eliminating the temperature gradient between hot side and cold side, the output voltage of 490 mV still can be retained, indicating a relatively low self-discharging rate of ~0.012% for the initial open circuit voltage and good electrochemical stability of such TAIC. In addition, such thermally charging device can work at multiple charge/discharge modes. After thermal charging, the OCV slowly reaches ~0.62 V (Figure 6d). Impressively, when the external power supply is available, the device can be galvanostatically recharged from thermally charging state (0.62 V) to the fully charged state (1.8 V). It is worth mentioning that the operation of thermal charging process has almost no effect on the subsequent galvanostatic charging/discharging process. Inspired by this finding, several charging-discharging cycles with hybrid charging mode can be realized (Figure 6d), further demonstrating the superior durability of rGO-PI//NCNF TAIC.

To further investigate the application potential of the TAIC device in multifunctional electronics, we assembled a flexible quasi-solid-state TAIC device using a PAM-PAA/(NH$_4$)$_2$SO$_4$ gel electrolyte. As shown in Figure 7(a), the gel electrolyte formed by PAA and PAM exhibits high transparency and excellent flexibility. As-assembled quasi-solid-state TAIC under various bending states sustain nearly similar specific capacitance (around 102 F g^{-1} at 0.5 A g^{-1}), suggesting good flexibility of such device (Figure 7b). The charged quasi-solid-state TAIC
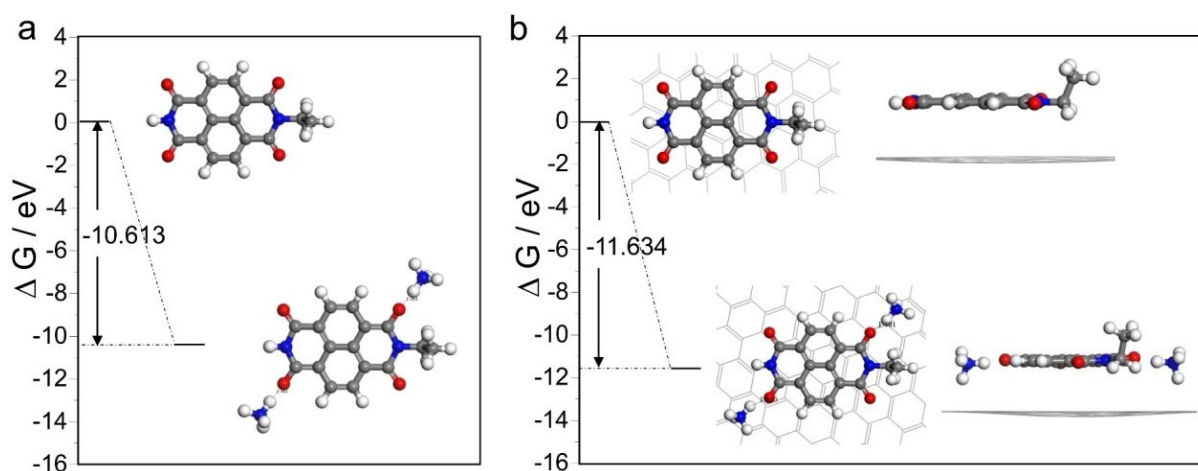
Figure 5. Free energies (ΔG) of a) PI and b) rGO-PI based on DFT calculations.

Figure 6. a) The galvanostatic discharge curves of TAIC at various temperature difference. b) The galvanostatic discharge curves of TAIC at various current density under 45 K. c) Self-discharge performance of TAIC after thermally charging to 624 mV. d) Charging/discharging behavior of the TAIC at thermally or/and galvanostatic charging hybrid modes and cycles.

device can maintain 0.936 V of the initial potential (1.8 V) after 120 h at standstill, meaning an ultralow self-discharge rate of 0.12 mV min^{-1} (Figure 7c). Which owing to slower ion transfer of gel electrolyte. In addition, the device with gel electrolyte can operate in a variety of temperatures and capacitance retention of ~95% can be maintained after 1000 cycles (Figure S12). As depicted in Figure S13 (Supporting information), the heat transfers from heating platform (positive electrode) to lower temperature electrode (negative electrode) and creates a controllable temperature gradient. Figure 7d shows thermally charging behavior of quasi-solid-state TAIC device at various temperature differences from 2.3 to 10.1 K. Notably, a high output voltage of ~100 mV can be achieved with a temperature difference of 10.1 K, which means an excellent thermopower of ~5.41 mV K^{-1}. When considering power output, the highest power density of 1.92 µW cm^{-2} can be retained for a fixed resistance only with one quasi-solid-state TAIC (Figure 7f). In addition, as shown in Figure 7(g), the quasi-solid-state TAIC can realize hybrid charging mode. As a demonstration, two quasi-solid-state TAICs after multiple charge modes connected in series as wearable devices could normally power two led lights (Figure 7h), illustrating the promising potential in practical application.

Conclusion

In summary, we have proposed a high-performance aqueous ammonium ion capacitor by using redox-active organic rGO-PI composite and NCNF for energy storage and low-grade heat conversion. Benefitting from the unique microstructure and physiochemical characteristics of electrodes, as-constructed devices exhibit satisfying performances such as capacitance, rate capability and thermopower. As a result, the rGO-PI//NCNF device displays a high energy density of 45.9 Wh kg^{-1} and a good cycling stability of ~94% capacitance retention over 10000 cycles at a current density of 5 A g^{-1}. Furthermore, the device can realize a high Seebeck coefficient as high as of 9.07 mV K^{-1} and output voltage of 624 mV. When loading an external resistance of 2 kΩ, the TAIC can output a power density of 82 µW cm^{-2}. Meanwhile, the assembled wearable quasi-solid-state device with gel electrolyte can well operate at various bending states. Such thermal charging devices have the following advantages: i) facile and low-cost strategy, ii) high heat-to-current conversion efficiency, iii) excellent energy storage performance. These findings open a way for the construction of high-performance device in thermoelectric conversion area, and will inspire emerging development of promising devices with high efficiency and prolonged durability.

Experimental Section

Preparation of NCNF and rGO-PI composite

Firstly, graphite oxide (GO) was prepared by a modified Hummers method. The rGO-PI composite was prepared through a high temperature polycondensation reaction and annealing process. Typically, 40 mg of GO powder was dispersed in 25 mL of *N*-methyl pyrrolidone (NMP) solvent by ultrasound for 30 min to form homogeneous GO dispersion. Subsequently, 0.40 g of 1,4,5,8-naphthalenetetracarboxylic dianhydride (NTCDA) and 0.09 g of
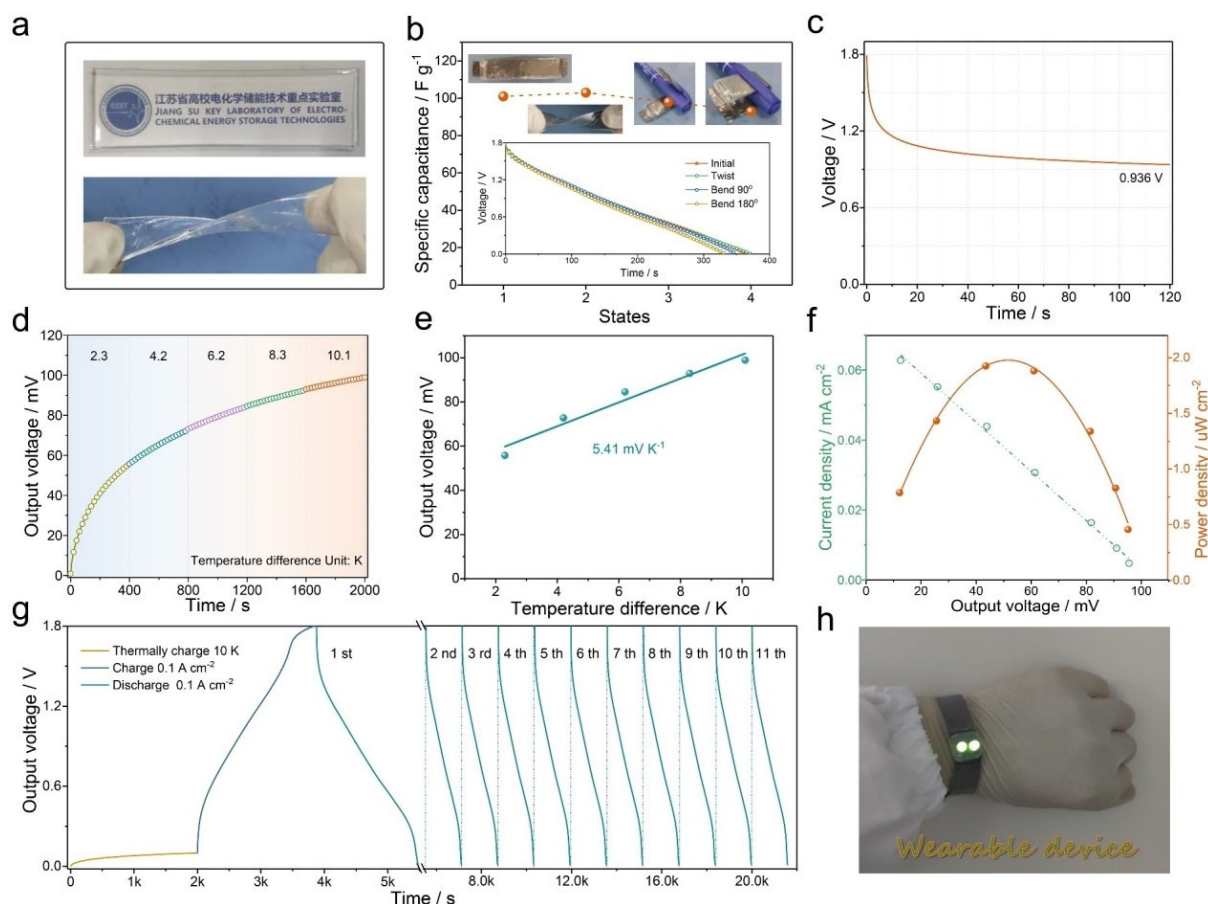
Figure 7. a) Digital photo of the as-prepared antifreeze gel electrolyte. b) Capacitance retention under of quasi-solid-state ammonium ion capacitor at various folding states (inset shows the corresponding discharge curves). c) Self-discharge curve of TAIC with gel electrolyte. d) Thermally charging process. e) A summary of ΔV and S at each temperature difference. f) Plots of power and current densities versus output voltage for the various load resistances at ΔT of 10.1 K. g) Charging/discharging behavior of the TAIC with gel electrolyte at thermally or/and galvanostatic charging hybrid modes and cycles. h) Digital photo of flexibility wearable TAIC with gel electrolyte.

ethylenediamine (EDA) were dissolved in the above dispersion part by part. After stirring at room temperature for 4 h, the poly-condensation reaction was proceed at 200 °C under the protection of nitrogen atmosphere for 8 h. The resulting mixture was collected and washed several times with methanol and NMP, respectively, and the product was dried under vacuum at 120 °C. Finally, the as-prepared product was calcined at 300 °C under nitrogen protection for 8 h to remove the residual solvent, denoted as rGO-PI. The pure PI and rGO were obtained through the same procedure of rGO-PI without the addition of GO or organic monomers, respectively. N-doped carbon nanofiber (NCNF) was prepared according to our previous report.[4]

Preparation of PAM-PAA-based anti-freeze gel electrolyte

The anti-freezing gel electrolyte was prepared through a UV-assisted polymerization. Firstly, $(NH_4)_2SO_4$ (1.5 g) was dissolved a mixed solution of ethylene glycol and distilled water (2:1, V/V) at room temperature. Then, acrylamide (AM, 2 g), acrylic acid (AA, 0.4 g), N,N-methylenebisacrylamide (MBA, 1.5 mg), N,N,N,N-tetramethylethylenediamine (TMDA, 10 μL) and $(NH_4)_2S_2O_8$ (0.25 g) were added into the above solution, respectively, with continuous stirring for 2 h under ice bath until the formation of transparent and uniform solution. Finally, appropriate amount of solution was infused into a mold to form the transparent antifreeze gel electrolyte through a UV lamp (365 nm, 60 W).

The processes of materials characterizations and electrochemical measurements are presented in the Supporting Information.

Supporting Information

Supporting Information is available from the Wiley Online Library or from the author.

Acknowledgements

Conflict of Interest

The authors declare no conflict of interest.

Data Availability Statement

The data that support the findings of this study are openly available in Batteries & Supercaps at https://doi.org/10.1002/batt.202200000, reference number 51.

[1] M. Bohlayer, G. Zoettl, *Energy* **2018**, *159*, 327–343.
[2] D. Silva, R. Cesar, M. Moreira, H. Santos, D. Souza, B. M. Pires, G. Lindomar, B. Pires, *Energy Storage Mater.* **2020**, *27*, 555–590.
[3] Z. Li, Y. Xu, L. Wu, Y. An, Y. Sun, T. Meng, H. Dou, Y. Xuan, X. Zhang, *Nat. Commun.* **2022**, *13*, 132.
[4] Y. An, Z. Li, Y. Sun, Z. Chen, J. Jiang, H. Dou, X. Zhang, *Energy Environ. Mater.* **2021**, DOI: 10.1002/eem2.12305.
[5] L. Fan, K. Lin, J. Wang, R. Ma, B. Lu, *Adv. Mater.* **2018**, *20*, 1800804.
[6] R. Koyama, L. Chen, S. Alavi, *Energy* **2020** *198*, 117403–117414.
[7] C. Forman, I. Muritala, R. Pardemann, B. Meyer, *Renewable Sustainable Energy Rev.* **2016**, *57*, 1568–1579.
[8] L. Bell, Cooling, heating, *Science* **2008**, *12*, 1457–1461.
[9] H. Nguyễn, . Lu, H. Goto, R. Maeda, *Nano Energy* **2018**, *49*, 172–178.
[10] W. He, D. Wang, H. Wu, Y. Xiao, Y. Zhang, L. Zhao, *Science* **2019**, *365*, 1418–1424.
[11] S. Maye, H. Girault, P. Peljo, *Energy Environ. Sci.* **2020**, *13*, 2191–2200.
[12] C. Han, X. Qian, Q. Li, B. Deng, Y. Zhu, Z. Han, G. Chen, W. Liu, *Science* **2020**, *368*, 1091–1098.
[13] A. Rattner, S. Garimella, *Energy* **2011**, *36*, 6172–6183.
[14] H. Lu, L. Price, Q. Zhang, *Appl. Energy* **2016**, *161*, 497–511.
[15] J. Duan, G. Feng, B. Yu, J. Li, M. Chen, P. Yang, J. Feng, K. Liu, J. Zhou, *Nat. Commun.* **2018**, *9*, 5146–5154.
[16] X. Wang, Y. Huang, C. Liu, K. Mu, K. Li, S. Wang, Y. Yang, L. Wang, C. Su, S. Feng, *Nat. Commun.* **2019**, *10*, 4151–4159.
[17] J. Duan, B. Yu, L. Huang, B. Hu, M. Xu, G. Feng, J. Zhou, *Joule* **2021**, *5*, 768–779.
[18] D. Zhao, H. Wang, Z. Khan, J. Chen, R. Gabrielsson, M. Jonsson, M. Berggren, X. Crispin, *Energy Environ. Sci.* **2016**, *9*, 1450–1458.
[19] Y. Liu, H. Wang, P. Sherrell, L. Liu, Y. Wang, J. Chen, *Adv. Sci.* **2021**, *8*, 2100669.
[20] K. Kim, J. Kang, H. Lee, *Chem. Eng. J.* **2021**, *426*, 131797.
[21] Z. Song, H. Zhan, Y. Zhou, *Angew. Chem. Int. Ed.* **2010**, *45*, 8444–8448.
[22] Z. Song, T. Xu, M. Gordin, Y. Jiang, I. Bae, Q. Xiao, H. Zhan, J. Liu, D. Wang, *Nano Lett.* **2012**, *12*, 2205–2211.
[23] Y. Huang, K. Li, J. Liu, X. Zhong, X. Duan, I. Shakirc, Y. Xu, *J. Mater. Chem. A* **2017**, *5*, 2710–2718.
[24] Y. Zhang, Y. An, B. Yin, J. Jiang, S. Dong, H. Dou, X. Zhang, *J. Mater. Chem. A* **2019**, *7*, 11314–11321.
[25] Y. Lu, J. Chen, *Nat. Chem. Rev.* **2020**, *4*, 127–142.
[26] Y. Xu, M. Zhou, Y. Lei, *Mater. Today* **2018**, *21*, 60–78.
[27] F. Disalvo, *Science* **1999**, *285*, 703–706.
[28] F. Bonaccorso, L. Colombo, G. Yu, M. Stoller, V. Pellegrini, *Science* **2015**, *347*, 1246501.
[29] L. Zhao, S. Lo, Y. Zhang, H. Sun, G. Tan, C. Uher, *Nature* **2014**, *508*, 373–377.
[30] A. Geim, K. Novoselov, *Nat. Mater.* **2007**, *6*, 183–191.
[31] M. Pumera, *Chem. Soc. Rev.* **2010**, *39*, 4146–4157.
[32] P. Han, M. Cheng, D. Luo, W. Cui, H. Liu, J. Du, M. Wang, Y. Zhao, L. Chen, C. Zhu, J. Xu, *Energy Storage Mater.* **2020**, *24*, 486–494.
[33] Y. An, Y. Yang, Z. Hu, B. Guo, X. Wang, X. Yang, Q. Zhang, H. Wu, *J. Power Sources* **2017**, *337*, 45–53.
[34] Y. Zhang, Y. An, L. Wu, H. Chen, Z. Li, Hui Dou, V. Murugadoss, J. Fan, X. Zhang, X. Mai, Z. Guo, *J. Mater. Chem. A* **2019**, *7*, 19668–19676.
[35] Y. Liu, Y. Liu, Y. Yamauchi, Z. Alothman, Y. Kaneti, X. Wu, *Batteries & Supercaps* **2021**, *4*, 1867–1873.
[36] C. Chen, Z. Li, Y. Xu, H. Liao, L. Wu, H. Dou, X. Zhang, *Batteries & Supercaps* **2021**, *4*, 680–686.
[37] Z. Li, D. Chen, Y. An, C. Chen, L. Wu, Z. Chen, Y. Sun, X. Zhang, *Energy Storage Mater.* **2020**, *28*, 307–314.
[38] J. Wang, J. Tang, Y. Xu, B. Ding, Z. Chang, Y. Wang, X. Hao, H. Dou, X. Zhang, Y. Yamauchi, *Nano Energy* **2016**, *28*, 232–240.
[39] C. Li, W. Wu, S. Zhang, L. He, Y. Zhu, J. Wang, L. Fu, Y. Chen, Y. Wu, W. Huang, *J. Mater. Chem. A* **2019**, *7*, 4110–4119.
[40] S. Dong, Y. Wang, C. Chen, L. Shen, X. Zhang, *Nano-Micro Lett.* **2020**, *12*, 168.
[41] R. Sahoo, T. Lee, D. Pham, T. Luu, Y. Lee, *ACS Nano* **2019**, *13*, 10776–10786.
[42] H. Liu, L. Liao, Y. Lu, Q. Li, *Adv. Energy Mater.* **2016**, *7*, 1601248.
[43] D. Qiu, J. Guan, M. Li, C. Kang, J. Wei, Y. Li, Z. Xie, F. Wang, R. Yang, *Adv. Funct. Mater.* **2019**, *29*, 1903496.
[44] S. Wang, W. Quan, Z. Zhu, Y. Yang, Q. Liu, Y. Ren, X. Zhang, R. Xu, Y. Hong, Z. Zhang, K. Amine, Z. Tang, J. Lu, J. Li, *Nat. Commun.* **2017**, *8*, 627–635.
[45] Y. Shabangoli, M. Rahmanifar, M. El-Kady, A. Noori, M. Mousavi, R. Kaner, *Adv. Energy Mater.* **2018**, *8*, 8 1802869.
[46] Y. Liu, C. Gao, S. Sim, M. Kim, S. Lee, *Chem. Mater.* **2019**, *31*, 4379–4384.
[47] A. Kazim, A. Booeshaghi, S. Stephens, B. Cola, *Sustain. Energy Fuels* **2017**, *1*, 1381–1390.
[48] J. Duan, G. Feng, B. Yu, J. Li, M. Chen, P. Yang, J. Feng, K. Liu, J. Zhou, *Nat. Commun.* **2018**, *9*, 5146–5154.
[49] S. Jung, J. Kwon, J. Lee, K. Shim, D. Park, T. Kim, Y. Kim, S. Hwang, Y. Kim, *ACS Appl. Energ. Mater.* **2020**, *3*, 6383–6390.
[50] Q. Shen, Z. Ning, B. Fu, S. Ma, Z. Wang, L. Shu, L. Zhang, X. Wang, J. Xu, P. Tao, C. Song, J. Wu, T. Deng, W. Shang, *J. Mater. Chem. A* **2019**, *7*, 6514–6522.
[51] S. Ahualli, M. Fernandez, G. Iglesias, A. Delgado, M. Jimenez, *Environ. Sci. Technol.* **2014**, *48*, 12378–12385.